

# Compressive strength and elastic properties of a transversely isotropic calcareous mudstone

Douglas Miller<sup>1,\*</sup> Richard Plumb<sup>2</sup> and Gregory Boitnott<sup>3</sup>

<sup>1</sup>Miller Applied Science LLC and MIT Department of Earth, Atmospheric and Planetary Sciences, <sup>2</sup>Plumb Geomechanics LLC and MIT Department of Civil and Environmental Engineering, <sup>3</sup>New England Research

Received March 2012, revision accepted December 2012

## ABSTRACT

This paper reports measurements of static and dynamic elastic properties plus compressive strength performed on a block of calcareous mudstone retrieved from an exploration well. Measurements of mechanical properties indicate that the mudstone is anisotropic with respect to all three properties. A detailed analysis of the elastic moduli computed using small unload reload cycles and simultaneous ultrasonic wave velocities shows both strong anisotropy and strong anelasticity. Surprisingly, the measurements are consistent with a mathematical description of a special type of anisotropic linear viscoelastic medium that is obtained by adding a set of compliant elements (e.g., contacts between clay particles, kerogen lenses, or micro-fractures) to an isotropic viscoelastic solid. This medium is fully characterized by density plus four parameters defining the viscoelastic solid and the excess normal compliance associated with the compliant elements. The mathematical model predicts a full set of parameters characterizing a transversely isotropic medium with a vertical axis of symmetry (a ‘tiv’ medium) for both low- and high-strain rate behaviour.

**Key words:** Anisotropic, Viscoelastic, Isotropic.

## INTRODUCTION

This study describes and analyses measurements made on a block of mudstone recovered from the top-hole section of a difficult-to-drill exploration well during a hole cleaning operation. Wellbore instability in shale and mudstone is not news. But, it is unusual that large samples of the problem formation are retrieved from an exploration well. When a driller is faced with wellbore instability, the first thing he wants to know is what mud weight should be used to stop it. Answering this question requires information about the mechanical properties and the state of stress in the problem formations, or at least a reasonable approximation of them. For the case in question, there were no logs or cores from anywhere on

the structure. So our rock sample provided the first opportunity to characterize the mechanical properties of the problem formation.

It is widely accepted that fine-grained argillaceous rocks are anisotropic with respect to elastic moduli and compressive strength. Moreover, elastic moduli measured in standard triaxial compression tests are commonly found to be significantly smaller than those computed from bulk density and elastic wave velocities measured on the same rock either in the lab or in the field.

Most observations of shales, including ours, are consistent with the hypothesis that the medium is symmetric under rotation around an axis perpendicular to the horizontal bedding. Such media are generally termed ‘transversely isotropic’ (Amadei, Swolfs and Savage 1987; Jaeger, Cook and Zimmerman 2007) and often referred to as ‘TIV’ or ‘VTI’, the ‘V’ indicating that the symmetry axis is vertical. Crystals with hexagonal symmetry exhibit TIV elastic behaviour.

\*E-mail: demiller@mit.edu; demiller@millerappliedscience.com; rplumb@plumbgeomechanics.com; boitnott@ner.com

There is a rich literature analysing shales as anisotropic elastic media (e.g., Hornby *et al.* 1995; Amadei 1996; Hornby 1998; Sayers 2005; Suarez-Rivera *et al.* 2006). There is also substantial literature documenting the need to go beyond pure elasticity when comparing elastic measurements made at different temporal frequencies (e.g., Cheng and Johnson 1981; Spencer 1981; Jackson 1993; Lakes 1998; Shearer 2009). There is relatively little work combining the two contexts. Biot (1954) described the essential theoretical framework and applied it to isotropic and cubic media. A number of papers report measurements of VTI moduli from ultrasonic measurements made under varying loads (Lo, Coyner and Toksöz 1986; Hornby 1998; Dewhurst and Siggins 2006). Sarout and Gueguen (2008a, b) reported on ultrasonic measurements under various loading conditions and fitted a micromechanical model to the measurements but they evidently did not perform unload-reload cycles or analyse the quasi-static elastic behaviour of their stress-strain curves. Sone (2012) reported both quasi-static and ultrasonic measurements made on a variety of shale samples but did not convert the quasi-static measurements to moduli suitable for comparison with the ultrasonic moduli. Hofmann (2006) described both reload cycle measurements of quasi-static moduli as a function of cycle rate and ultrasonic measurements on the same pair of shale samples. Both sets of measurements were converted to comparable forms and 'significant dispersion effects between the low frequency and ultrasonic frequency range' were reported.

Our observations will be presented in a form that is as independent of theory and prior expectation as we can make it. However, discussion of the observations will be carried out in the context of linear viscoelasticity (e.g., Biot 1954; Lakes 1998; Carcione 2001; Shearer 2009). For pure linear elasticity, the coefficients in Hooke's law, which defines a linear relationship between stress and strains, are real and independent of the strain rate. Linear viscoelasticity admits anelasticity of a particularly tractable form: a linear viscoelastic medium satisfies a rate-dependent form of Hooke's law that can be thought of as a family of rate-dependent, complex-valued elastic tensors.

A key observable for all linearly viscoelastic materials is that stiffness is an increasing function of strain rate. Hofmann (2006) included a thorough survey of the literature related to anelastic properties of shales and analysed measurements on a pair of shale samples in a way that is similar to what we do here. Our study presents data on a mudstone with distinctly different composition and texture than those studied by Hofmann (2006). We also include some discussion, absent in Hofmann (2006), of possible mathematical regular-

ities connected to microstructural models. The observational parts of the present paper require little from viscoelasticity beyond the notion that elastic measurements of the same material at different strain rates may give different answers that reflect the same underlying morphological symmetry (e.g., VTI). Additional details will be reviewed in the discussion section.

Another seemingly important observation from our present study is that the slope of the cross-plot between axial stress and radial strain for reload cycles is, to experimental accuracy, identical when measured on plugs cut normal and parallel to bedding. This translates to an observation that there are only four independent VTI moduli (at the given strain rate) and that the material responds as an isotropic material to which horizontally aligned excess compliances have been added. Not all shales exhibit such behaviour. For example, Miller, Horne and Walsh (2012) described a complete set of sonic log measurements from a gas-shale formation that is, to experimental accuracy, inconsistent with this type of simplification. The simplification is, however, an important special case. For example, Sayers (2008) assumed this simplification when developing a theory of microstructural behaviour and applied this theory to a set of measurements of a muscovite sample by Alexandrov and Ryzhova (1961).

In the following sections we describe the rock, laboratory tests performed on it and an analysis of those measurements. Results of the mechanical testing are presented in two parts. The first part discusses the test protocol and basic observations concerning the static moduli and strengths as a function of confining pressure. Observations made within this context illustrate the interrelationships of key mechanical properties needed to build a geomechanical model for this material.

The second part of the paper makes a detailed analysis of measurements performed on one pair of plugs, comparing elastic properties estimated from unload-reload cycles with those estimated from ultrasonic tests. We find that the data for this particular pair exhibit both strong anisotropy and strong anelasticity. Both measurements detect that the material is stiffer in the plane of the bedding than in planes normal to bedding and the ultrasonics observe a stiffer medium than the quasi-static unload-reload cycles. The surprising observation is that the two phenomena appear to be linked: the ratio between the ultrasonic and quasi-static stiffnesses is the same as the ratio between the horizontal and vertical shear stiffnesses measured either way. Our observation is consistent with a physical model in which horizontally aligned excess compliances are added to a particular type of isotropic viscoelastic medium.



**Figure 1** Sample of the mudstone recovered from the exploration well. Marks indicate the location of the 20 mm plug samples cut parallel and perpendicular to the bedding.

The paper is by no means a comprehensive survey of strength, anisotropy and anelasticity in shales. In fact it is the opposite: it is a terse but reasonably complete examination of one particular mudstone. Figures show the sample as a whole, the locations where the plugs were cut, the data extracted from the plugs, as well as the fit of a model that has surprising but clearly observable regularity in its anelastic properties. Given the small number of measurements, we found it practical to display all the data used in the detailed analysis and to annotate them with extracted slopes, time picks and precisions. We invite the reader to directly compare the observed regularities, fits and misfits in order to judge their significance.

## ROCK CHARACTERIZATION

The rock described in this paper is a calcareous mudstone retrieved from the top-hole section of an exploration well during a hole cleaning operation (Fig. 1). Several blocks of rock like the one shown in Fig. 1 comprise two textures: a calcareous mudstone and fine-grained calcareous grainstone. The focus of this paper is the mudstone as it was responsible for the majority of the wellbore instability problems. Two mudstone blocks (denoted '1a' and '1b') were processed to obtain three 20 mm diameter plugs from each. Figure 1 shows block 1b with markings indicating the locations where plugs 1bv1 (perpendicular to the bedding) and 1bh1a (parallel to the bedding) were obtained. In order to orient the plugs properly, pieces were trimmed from the samples, hand polished and examined by a scanning electron microscope. Hand polishing with a small amount of water was found to enhance the exposure

of the grain-scale fabric of the mudstone. This observation ensured that the plugs were cut parallel and normal to the depositional fabric (bedding). After preparation, these two plugs were respectively 34.5 mm and 42.3 mm long.

Figure 2 shows backscattered electron microscope images of the mudstone taken at three different magnifications. Bedding, visible in all three images, is defined by pyrite nodules (bright components).

Modal mineralogy, expressed as per cent by weight, was measured using a scanning energy dispersive X-ray system. The mineral assemblages obtained for the mudstone samples cut parallel and perpendicular to bedding were similar to each other whereas those of the mudstone and the grainstone were distinctly different (Table 1).

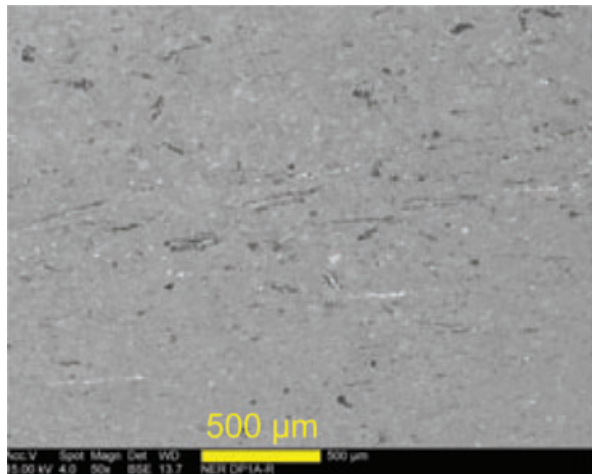
Figure 3 shows a mineral map of a 4 cm × 9 cm section of the mudstone. The map demonstrates that smectite clay minerals form the continuous, load-bearing solid phase in the mudstone (olive green). Floating in the clay are grains of serpentine (brown), calcite and dolomite (blues). There is little illite and no significant cementation.

The porosity estimated for the mudstone is approximately 9%. Porosity was computed from measurements of grain density and bulk density. Plug ends were used to obtain a measure of grain density. They were crushed, pulverized and then vacuum oven dried at 110°C prior to testing in a helium pycnometer. These density porosities may be slightly underestimated because they neglect effects of adsorbed water in the plug samples (room dry condition).

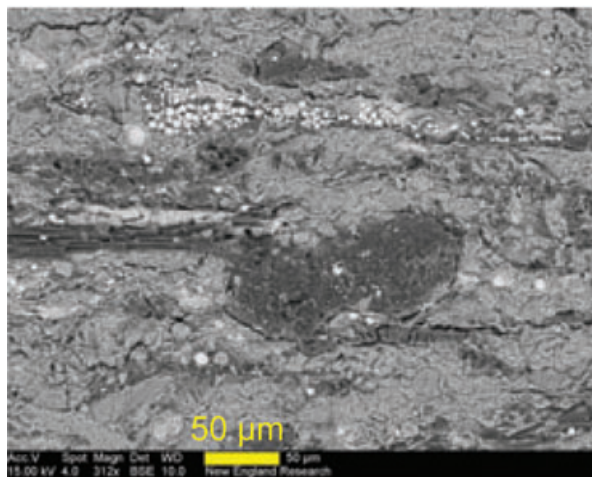
## MECHANICAL TESTING

The primary objective of the laboratory testing was to measure the parameters required by standard geomechanics software: Young modulus, Poisson ratio, unconfined compressive strength and friction angle. Toward this end, axial compression tests to failure were run at confining pressures of 0 MPa, 20 MPa and 40 MPa according to ISRM standards (Brown 1981). One vertical and one horizontal plug were processed at each confining stress. The plugs indicated in Fig. 1 were tested at 0 MPa confining pressure. Compression tests to failure were performed on room dry samples.

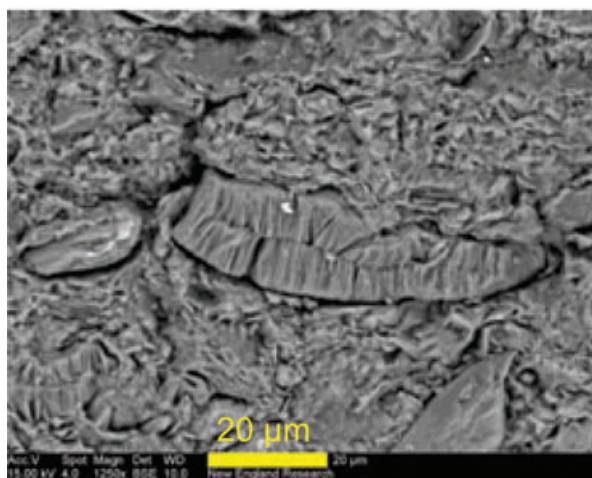
Tests were conducted using a New England Research Autolab 1500 system. Figure 4 shows some of the details of the system, which is designed to acquire axial ultrasonic measurements while monitoring stress and strain under servo-controlled confining pressure and axial differential loading. Axial loading at fixed confining pressure was controlled in displacement feedback. Results from a similar system were



(a)



(b)



(c)

**Table 1** Mineralogy determined by a scanning energy dispersive X-ray system. All reported values are per cent by weight.

| Mineral    | Calcareous Mudstone |               | Carbonate Grainstone |               |
|------------|---------------------|---------------|----------------------|---------------|
|            | parallel            | perpendicular | parallel             | perpendicular |
| Quartz     | 2.6                 | 2.6           | 8.5                  | 8.3           |
| Calcite    | 12.8                | 15.3          | 36.2                 | 40.7          |
| Dolomite   | 1.2                 | 1.4           | 4.1                  | 4.0           |
| Albite     | 0.7                 | 0.8           | 1.6                  | 1.7           |
| K-feldspar | 2.9                 | 1.5           | 5.0                  | 3.8           |
| Illite     | 1.8                 | 0.9           | 0.8                  | 0.7           |
| Smectite   | 60.0                | 59.3          | 22.2                 | 19.7          |
| Serpentine | 14.7                | 14.7          | 17.3                 | 16.9          |
| Chlorite   | 1.7                 | 1.7           | 2.5                  | 2.6           |
| Pyrite     | 1.0                 | 1.2           | 0.6                  | 0.5           |
| Rutile     | 0.3                 | 0.4           | 0.2                  | 0.2           |
| Chromite   | 0.0                 | 0.0           | 0.4                  | 0.4           |
| Fe-oxides  | 0.0                 | 0.0           | 0.4                  | 0.3           |
| Others     | 0.3                 | 0.2           | 0.2                  | 0.2           |
| Total      | 100                 | 100           | 100                  | 100           |

reported by Sone (2012). Hofmann (2006, section 3.2.2) described and analyzed similar measurements made on a pair of shales of similar composition but dissimilar porosity (2.5% and 7.5%). The 9% porosity of our mudstone lies between these values. Hofmann's shales are mineralogically quite different from our mudstone, having significant amounts of quartz, kaolinite and illite and insignificant amounts of calcite and smectite.

Sample deformation was measured using strain gauges bonded directly to the plug sample. In the case of the unconfined compression tests, samples were instrumented with two axial and two radial strain gauges, each diametrically opposite the other similarly oriented gauge (Fig. 4). For tests at elevated confining pressure, only one radial gauge was used. For the horizontal plugs, radial gauges were oriented at 45° to the bedding to provide an average radial response. The active area of each gauge was 0.25" × 0.25" (6.35 mm × 6.35 mm). 22 mm diameter ultrasonic transducers were connected to tapered titanium endcaps to enable axial

**Figure 2** Backscattered Scanning Electron Microscope images of the mudstone sample: (a) 50× magnification showing homogeneous texture and traces of bedding; (b) 312× magnification showing bedding defined by organic matter (dark) and pyrite nodules (bright) but no cementation; (c) 1250× magnification showing a high-volume fraction of clay minerals. Some of the porosity, visible at the boundaries between different mineral phases, may be artefacts of unloading.

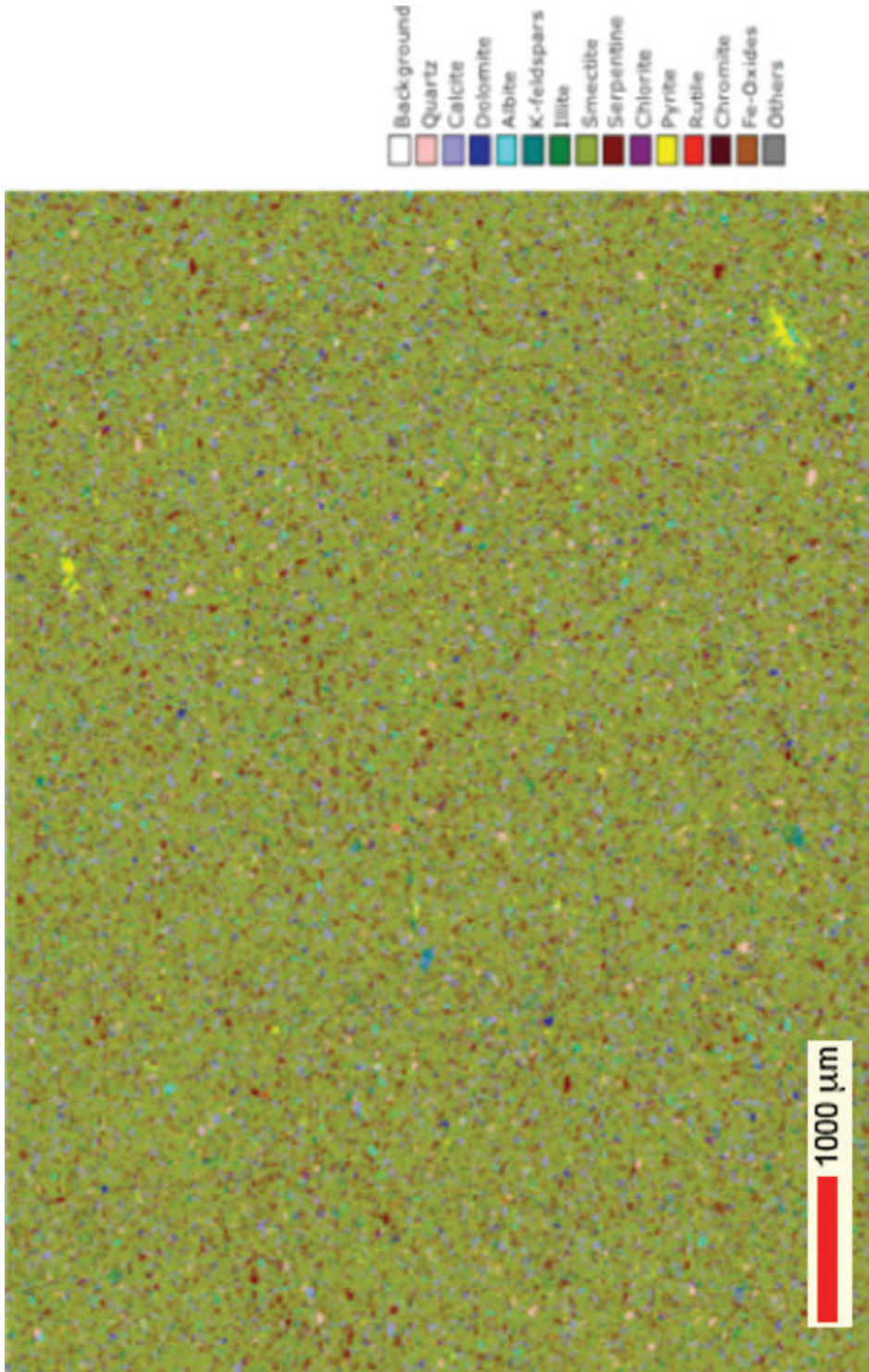


Figure 3 Mineral composition map of the mudstone illustrating the homogeneous nature of the rock at the centimetre scale.

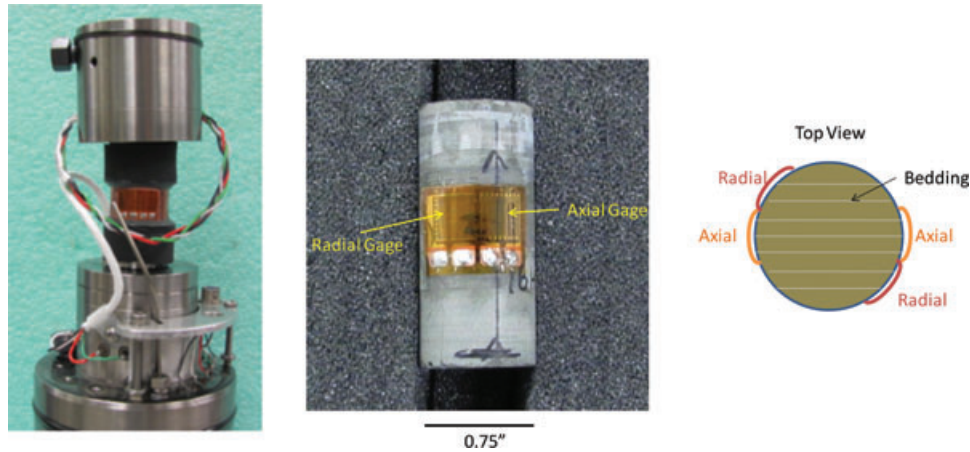


Figure 4 Photograph of a sample stack (left), a close-up photograph of a gauged sample (centre) and a diagram of sample instrumentation for a horizontal sample (right). For vertical samples, the gauge pattern was similar but placement was with respect to an arbitrary direction.

compressional and orthogonally polarized shear propagation speed measurements.

A similar test protocol was carried out on each plug. Figure 5 shows the stress-strain cross-plot for the protocol as run on the pair tested at zero-confining pressure. Periodic small amplitude (5 MPa) unload-reload cycles were performed to obtain a measure of reloading moduli as a function of deformation. Ultrasonic velocities were measured prior to each unloading cycle, providing a comparison of dynamic moduli, calculated from ultrasonic data, with the quasi-static loading and reloading moduli. The duration of the run was about 1 hour. Unload-reload cycles were of about 4 minutes duration.

Relative to the reload cycle measurements, the ultrasonic measurements have significantly lower strain amplitudes (roughly  $3E-7$  for ultrasonics,  $2E-4$  for reload cycles)

but significantly higher strain rates (roughly  $100\text{ s}^{-1}$  for ultrasonics,  $4E-6\text{ s}^{-1}$  for reload cycles). A detailed discussion of the ultrasonic and reload-cycle data will be given in the next section.

Compressive strengths were measured by manually identifying the maximum differential axial stress attained during the test. Samples were taken at various stages of post failure depending on particular circumstances of the test.

Strength results are summarized graphically in Fig. 6. Strengths plotted in Mohr-Coulomb space yield two linear and parallel failure envelopes, with a suggestion of downward curvature in the horizontal plugs at the highest stresses. The slope of the envelopes, known in rock mechanics literature as the ‘angle of internal friction’, (e.g., Jaeger *et al.* 2007, section 4.5) is 22 degrees.

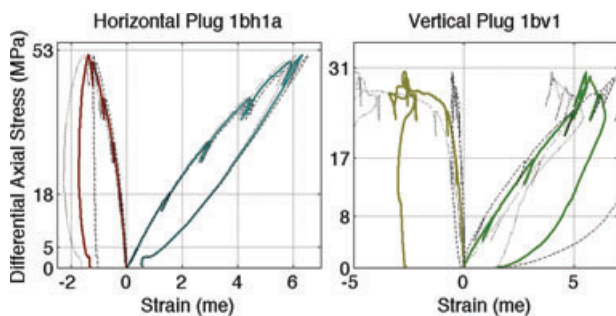


Figure 5 Example of stress versus strain results for a typical pair of tests. Tick marks on the vertical axis indicate the differential axial strain levels where ultrasonic recordings and unloading cycles were performed. Black dashed and dotted curves are from individual strain gauges. Coloured curves show the average response of each of the redundant pair of gauges.

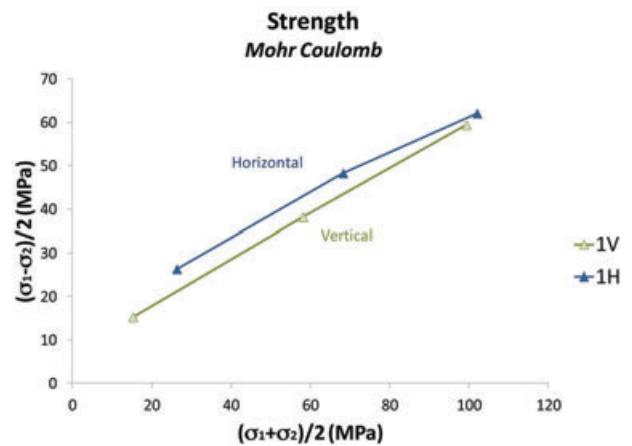


Figure 6 Measured strengths (shear stress at failure) as a function of normal stress.

**Table 2** Summary of test results. Plugs labelled 1\*v\* are cut perpendicular to the bedding. Plugs labelled 1\*h\* are cut parallel to the bedding.

| Plug  | Confining Pressure (MPa) | Compressive Strength (MPa) | Load                |               | Unload-Reload       |               |
|-------|--------------------------|----------------------------|---------------------|---------------|---------------------|---------------|
|       |                          |                            | Young Modulus (GPa) | Poisson Ratio | Young Modulus (GPa) | Poisson Ratio |
| 1bv1  | 0                        | 31                         | 4.6                 | 0.06          | 9.1                 | 0.09          |
| 1av1  | 20                       | 76                         | 4.9                 | 0.12          | 13.4                | 0.18          |
| 1av2  | 40                       | 119                        | 4.9                 | 0.11          | 14.3                | 0.22          |
| 1bh1a | 0                        | 53                         | 9.1                 | 0.19          | 15.3                | 0.17          |
| 1ah1  | 20                       | 97                         | 8.9                 | 0.06          | 16.7                | 0.17          |
| 1bh1b | 40                       | 124                        | 7.6                 | 0.07          | 15.4                | 0.15          |

A summary of the conventional rock mechanical parameters derived from the tests is shown in Table 2. The results exhibit the expected anisotropy with respect to loading direction, with the horizontal plugs yielding systematically greater Young moduli and compressive strengths than the vertical plugs. Note that the tabulated Young moduli and Poisson ratios were calculated directly from slopes of the load or reload cross-plots and, while they need to be properly interpreted, no assumption of isotropy was used in this calculation.

In summary we find for the mudstone:

- The compressive strength is greater measured parallel to bedding than perpendicular to it.
- All measured elastic moduli are greater measured parallel to bedding than perpendicular to it.
- Both the Young modulus and Poisson ratio are greater when measured on unload-reload cycles than when measured by the tangent to the initial load curve.
- There is a strong dependence of compressive strength on confining pressure whereas the dependence of elastic moduli on confining pressure is relatively weak.
- The magnitude of anisotropy in the unload-reload Young modulus decreases with increasing confining pressure.

In the next section, we will focus on the constitutive properties of the mudstone as measured at zero-confining pressure.

## CALCULATION OF ANISOTROPIC ELASTIC MODULI

In this section we will make a detailed comparative analysis of the elastic behaviour of the pair of plugs 1bv1 (perpendicular to the bedding) and 1bh1a (parallel to the bedding) as tested at about 15 MPa differential axial load and zero radial load. It is the pair with the most complete set of measurements and with the closest match between the locations where the plugs were cut. We will first attempt to summarize the observations

on this pair of plugs in a way that is as neutral as possible with respect to prior expectations. Next we will identify a simple mathematical model (with four free parameters) that is consistent with the observed data.

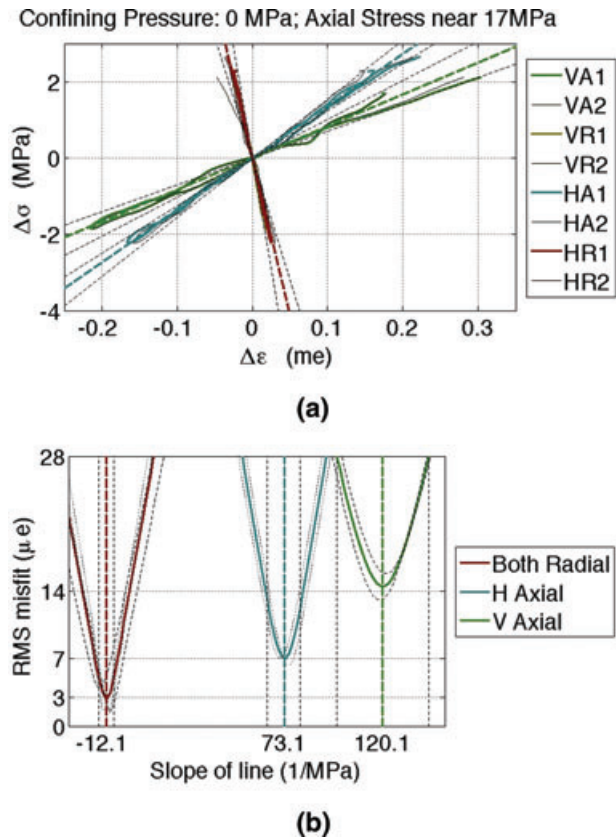
## Observations

Figure 7(a) shows the reloading cycles closest to 17 MPa differential stress from the data shown in Fig. 5. Note that whereas the overall load curves are concave downwards and show significant variability between the redundant pairs of gauges, the reloading cycles are remarkably linear and consistent. There are eight cycles plotted in Fig. 7(a). They are difficult to distinguish because the redundant pairs match remarkably well and because the radial cycles for the two plugs match each other.

Slopes in reload-cycle measurements on axial plugs under constant confining pressure are simply related to elastic compliances. Hofmann (2006) discussed general relations between gauge readings and components of a compliance tensor. For our simple set-up, the slopes labelled 'VA', 'VR' and 'HA' in our Fig. 7 correspond directly to  $S_{33}$ , and  $S_{11}$ . The radial measurement 'HR' that was made at 45° to the bedding on the horizontal plug is slightly more complicated (Hofmann 2006, Table 3.2): it corresponds to the average of  $S_{13}$  with  $S_{12}$ . Thus, the observed match between the radial cycles for the two plugs leads to a conclusion that  $S_{12} = (S_{12} + S_{13})/2$  and hence that  $S_{12} = S_{13}$ .

Table 3 summarizes the compliance values determined from the slopes shown in Fig. 7. Precision estimates in Table 3 match the width of the zones indicated by dotted lines in Fig. 7.

Figure 8 shows axial ultrasonic data recorded closest to the reloading cycles shown in Fig. 7. Since the recordings are made with plugs sandwiched between metal connection heads,



**Figure 7** (a) Reloading cycles nearest to 17 MPa for six strain gauges. VA1 and VA2 are axial gauges on the vertical plug. VR1 and VR2 are the radial gauges on the vertical plug, etc. (b) Root mean square (RMS) misfit as a function of the slope  $\Delta\epsilon/\Delta\sigma$  of lines approximating the reloading cycles shown in (a). Coloured dashed lines indicate best fit. Black dashed lines in both figures mark lines with the RMS misfit equal to twice that of the best fit.

**Table 3** Observed compliances and estimated precisions from the reload cycle data shown in Fig. 7.

| Compliance | Horizontal Plug |          |          | Vertical Plug |          | Units |
|------------|-----------------|----------|----------|---------------|----------|-------|
|            | $S_{11}$        | $S_{12}$ | $S_{66}$ | $S_{33}$      | $S_{13}$ |       |
|            | 73.1            | -12.1    | 170.5    | 120.1         | -12.1    | 1/MPa |
|            | ±8              | ±3.5     | ±7       | ±22           | ±3.5     |       |

the zero-time reference is established by picking time-breaks on waveforms (shown in brown and labelled ‘S0’, and ‘P0’) recorded with the heads in contact. For each plug and mode of propagation shown in Fig. 7, the associated amplitude-normalized waveform is plotted as a function of normalized propagation time – each time sample has been scaled by the reciprocal of the plug length. Thus, the apparent delay is ex-

actly proportional the reciprocal of the propagation speed (slowness) for the given mode and plug. For each plug and mode, three waveforms are plotted, the central waveform being the one recorded just before the reload cycle closest to 17 MPa. The adjacent waveforms were recorded just before the preceding and following reload cycles. The first index on the trace labels indicates plug orientation, the second index labels polarization. Thus, ‘11’ labels the compressional measurement on the horizontal plug, ‘13’ is the vertically polarized shear on the horizontal plug, etc.

The dotted lines give the conservative estimates of the precision of the estimated velocities. Note that three sets of waveforms, labelled ‘13’, ‘31’, and ‘32’, which are respectively the vertically polarized shear on the horizontal plug and the two orthogonally polarized shears on the vertical plug, all have essentially the same wave speed. The match of 31 with 32 is clear evidence for transverse isotropy. The roughly 4% mismatch between the slow shear on the horizontal plug and both shears on the vertical plug is likely to be the combined result of sample heterogeneity and the different effect of axial loading on the two plugs. In view of the apparent stress sensitivity of the shear on the vertical plug and lack thereof on the horizontal plug, the response to loading appears to be the stronger effect.

Ultrasonic measurements are simply related to elastic moduli. The diagonal elements of the stiffness matrix  $C_{ij}$  are related to the squared speeds for wave propagation in the vertical and horizontal directions. For velocities, we use the convention that the first subscript indicates the direction of propagation and the second subscript indicates the direction of polarization.  $V_{11} = \sqrt{C_{11}/\rho}$  is the wave speed for horizontally propagating compressional vibration;  $V_{12} = \sqrt{C_{66}/\rho}$ , the wave speed for horizontally propagating shear vibration with horizontal polarization;  $V_{31} = V_{13} = \sqrt{C_{55}/\rho}$ , the wave speed for vertically propagating shear vibration, as well as for horizontally propagating shear vibration with vertical polarization;  $V_{33} = \sqrt{C_{33}/\rho}$ , the wave speed for vertically propagating compressional vibration.

Table 4 summarizes the velocities estimated from the waveforms in Fig. 8, together with precision estimates and the computed moduli. Precision estimates in Table 4 match the width of the zones indicated by the dotted lines in Fig. 8.

## COMPLIANCES AND MODULI

This section examines relationships between the compliances determined from the reload cycles and the velocities measured from the ultrasonic data. Using Voigt notation (Voigt 1928;

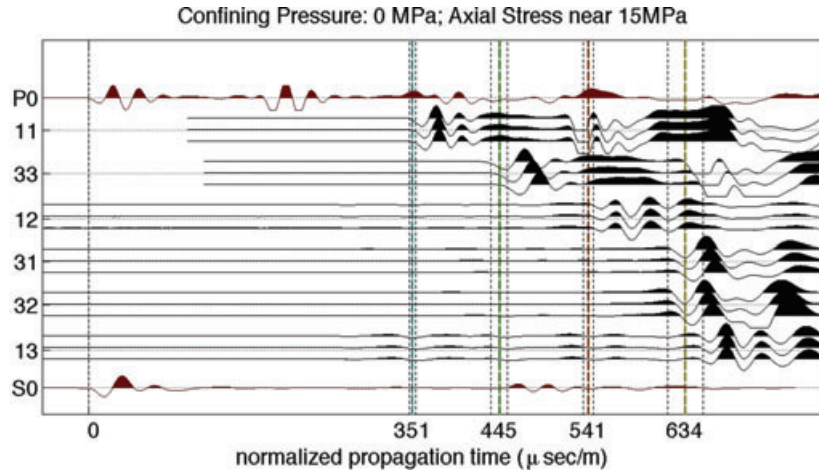


Figure 8 Ultrasonic data. The central waveform in each group was recorded just before a reload cycle at 17 MPa, shown in Fig. 7. The 1st index on the trace labels (left of the plot) indicates plug orientation and the 2nd index labels polarization.

Table 4 Observed velocities, estimated precisions and calculated moduli from the ultrasonic data shown in Fig. 8.

| Velocity | Horizontal Plug  |                  |                 | Vertical Plug    |                  |                  | Units |
|----------|------------------|------------------|-----------------|------------------|------------------|------------------|-------|
|          | $V_{11}$         | $V_{12}$         | $V_{13}$        | $V_{33}$         | $V_{31}$         | $V_{32}$         |       |
|          | $2.852 \pm 0.03$ | $1.849 \pm 0.04$ | $1.519 \pm .06$ | $2.248 \pm 0.03$ | $1.580 \pm 0.06$ | $1.576 \pm 0.06$ | km/s  |
| Modulus  | $C_{11}$         | $C_{66}$         | $C_{55}$        | $C_{33}$         | $C_{55}$         | $C_{44}$         |       |
|          | 19.4             | 8.14             | 5.49            | 12.0             | 5.94             | 5.91             | GPa   |

Jaeger *et al.* 2007) as above, Hooke's law can be written either in terms of a stiffness matrix  $\mathcal{C}$  giving stresses as a function of strains:

$$\begin{bmatrix} \sigma_{11} \\ \sigma_{22} \\ \sigma_{33} \\ \sigma_{23} \\ \sigma_{13} \\ \sigma_{12} \end{bmatrix} = \begin{bmatrix} C_{11} & C_{12} & C_{13} & & & \\ C_{12} & C_{22} & C_{23} & & & \\ C_{13} & C_{23} & C_{33} & & & \\ & & & C_{44} & & \\ & & & & C_{55} & \\ & & & & & C_{66} \end{bmatrix} \begin{bmatrix} \epsilon_{11} \\ \epsilon_{22} \\ \epsilon_{33} \\ 2\epsilon_{23} \\ 2\epsilon_{13} \\ 2\epsilon_{12} \end{bmatrix}, \quad (1)$$

or in terms of a compliance matrix  $\mathcal{S}$  giving strains as a function of stresses

$$\begin{bmatrix} \epsilon_{11} \\ \epsilon_{22} \\ \epsilon_{33} \\ 2\epsilon_{23} \\ 2\epsilon_{13} \\ 2\epsilon_{12} \end{bmatrix} = \begin{bmatrix} S_{11} & S_{12} & S_{13} & & & \\ S_{12} & S_{22} & S_{23} & & & \\ S_{13} & S_{23} & S_{33} & & & \\ & & & S_{44} & & \\ & & & & S_{55} & \\ & & & & & S_{66} \end{bmatrix} \begin{bmatrix} \sigma_{11} \\ \sigma_{22} \\ \sigma_{33} \\ \sigma_{23} \\ \sigma_{13} \\ \sigma_{12} \end{bmatrix}. \quad (2)$$

The above expressions are the general form for a medium in which each coordinate plane is a plane of mirror symmetry (an 'orthotropic medium'). When the medium is VTI, the additional relations:

$$\begin{aligned} C_{44} &= C_{55}, & C_{11} &= C_{22}, & C_{13} &= C_{23}, \\ C_{11} &= C_{12} + 2C_{66}, \\ S_{44} &= S_{55}, & S_{11} &= S_{22}, & S_{13} &= S_{23}, \\ S_{11} &= S_{12} + S_{66}/2, \end{aligned} \quad (3)$$

are satisfied and the nine independent parameters are reduced to five. Some of them have names and common abbreviations in engineering literature (e.g., Amadei *et al.* 1987).  $1/S_{11}$ , commonly abbreviated to  $E$ , is the 'Young modulus in the plane of isotropy'.  $1/S_{33}$ , commonly abbreviated to  $E'$ , is the 'Young modulus normal to the plane of isotropy'.  $-S_{13}/S_{33}$ , commonly abbreviated to  $\nu'$ , is the 'Poisson ratio normal to the plane of isotropy.'  $C_{66}$ , commonly abbreviated to  $G$  or  $\mu$ , is the 'shear modulus in the plane of isotropy', etc. We will use the terms 'modulus' and 'stiffness' as synonyms and we will refer to the

3 × 3 upper left block of  $\mathcal{C}$  or  $\mathcal{S}$  as the ‘compressional block’ and the diagonal 3 × 3 lower right block as the ‘shear block’.

When written as in equations (1) and (2), the modulus and compliance tensors are matrix inverses to one another:

$$[S_{ij}] = [C_{ij}]^{-1}. \tag{4}$$

Because the shear block of each matrix is diagonal, the shear moduli and shear compliances are reciprocals of one another:

$$S_{44} = C_{44}^{-1}, \quad S_{55} = C_{55}^{-1}, \quad S_{66} = C_{66}^{-1}. \tag{5}$$

The equations for compressional moduli in terms of compressional compliances are more complicated but can be simply derived from the expression for the matrix inverse from the compressional block of equation (2), combined with simplifications resulting from the VTI symmetries equation (3). They are (Jaeger *et al.* 2007; Lubarda 2008, section 5.10):

$$C_{11} = \frac{S_{11} - S_{13}^2/S_{33}}{S_{11} - S_{12}} C, \tag{6}$$

$$C_{12} = -\frac{S_{12} - S_{13}^2/S_{33}}{S_{11} - S_{12}} C, \tag{7}$$

$$C_{13} = -\frac{S_{13}}{S_{33}} C, \tag{8}$$

$$C_{33} = \frac{S_{11} + S_{12}}{S_{33}} C, \tag{9}$$

where

$$C = \frac{1}{S_{11} + S_{12} - 2S_{13}^2/S_{33}}. \tag{10}$$

The above equations are for calculating moduli from given compliances. To calculate compliances from moduli, one simply interchanges the letters ‘C’ and ‘S’ in all expressions. We will refer to these dual equations as (S6)–(S10).

Using these equations, the compliances measured by the reload cycles can be converted to moduli for comparison with those derived from the ultrasonic data. Table 5 summarizes this comparison (units are GPa).

The comparison is both striking and puzzling. There is a highly significant mismatch between the values that are computed twice, i.e., from both reload cycles and ultrasonics. While it is not surprising that the ultrasonics observe a stiffer medium than the reload cycles, the ratio between the reload and ultrasonic moduli is remarkably consistent and is quite close to the ratio  $C_{66} : C_{55}$  of shear moduli estimated from the ultrasonic data.

Table 5 Comparison of moduli calculated from reload cycles and from the ultrasonic data. Boldface values are cross-plotted as red dots in Fig. 9.

|            | $C_{11}$    | $C_{66}$    | $C_{33}$    | $C_{13}$ | $C_{55}$ |
|------------|-------------|-------------|-------------|----------|----------|
| Reload     | <b>14.4</b> | 5.87        | 8.67        | 1.72     |          |
| Ultrasonic | 19.4        | <b>8.14</b> | <b>12.0</b> |          | 5.70     |
| Ratio      | 1.35        | 1.39        | 1.38        |          |          |

Moduli from Table 5 are plotted in Fig. 9. The straight line fit to the moduli corresponds to a strict linear relationship:

$$C_{ij}^U = \phi C_{ij}^R, \tag{11}$$

with a value  $\phi = 1.40$ . The three red dots are a cross-plot of the moduli  $\{C_{11}, C_{66}, C_{33}\}$  from the first two rows of Table 5.

Table 6 summarizes the calculations for the moduli indicated by black symbols in Fig. 9. It enforces the relationship (11) plus the relationship:

$$\phi = C_{66}^U / C_{55}^U. \tag{12}$$

Our value for  $\phi$  was determined using a simple Matlab routine (lsqnonlin) to minimize the squared difference between the boldface measurements in Tables 3 and 4 and the corresponding values calculated from the moduli derived from equation (11) and listed in boldface in Table 6. Rows labelled ‘R’ fit the reload cycle measurements. Rows labelled ‘U’ fit the ultrasonic data. The calculated ratio (1.40) applies to all columns, as well as to the ratio  $C_{66}/C_{55}$  in either row. Calculated slownesses are included for comparison with Fig. 8. Note that the 1st subscript on the velocities indicates plug orientation, the 2nd subscript labels polarization whereas subscripts on moduli and compliances follow Voigt convention. Thus for example,  $V_{12}$  corresponds to  $C_{66}$  and  $V_{13}$  corresponds to  $C_{55}$ .

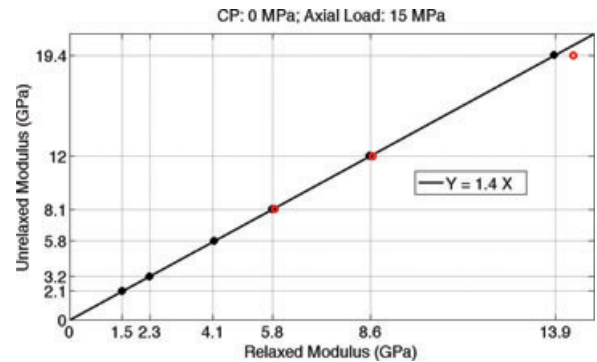


Figure 9 Cross-plot of measured reload and ultrasonic moduli. Red dots correspond to boldface moduli from Table 5.

**Table 6** Best-fit proportional moduli with compliances and velocities calculated from those moduli. Note that the first subscript on the velocities indicates plug orientation and the second subscript labels polarization whereas subscripts on moduli and compliances follow Voigt's convention.

| Moduli     | $C_{11}$   | $C_{12}$   | $C_{13}$   | $C_{33}$   | $C_{55}$   | $C_{66}$   | Units           |
|------------|------------|------------|------------|------------|------------|------------|-----------------|
| R          | 13.85      | 2.280      | 1.496      | 8.577      | 4.125      | 5.785      | GPa             |
| U          | 19.42      | 3.198      | 2.099      | 12.03      | 5.785      | 8.113      | GPa             |
| Ratio      | 1.402      |            |            |            |            |            |                 |
| Compliance | $S_{11}$   | $S_{12}$   | $S_{13}$   | $S_{33}$   | $S_{55}$   | $S_{66}$   |                 |
| R          | 75.25      | -11.12     | -11.12     | 120.5      | 242.4      | 172.9      | 1/MPa           |
| Velocity   | $V_{11}$   | $V_{12}$   | $V_{13}$   | $V_{33}$   | $V_{31}$   | $V_{32}$   |                 |
| U          | 2.857      | 1.846      | 1.559      | 2.248      | 1.559      | 1.559      | km/s            |
| Slowness   | $1/V_{11}$ | $1/V_{12}$ | $1/V_{13}$ | $1/V_{33}$ | $1/V_{31}$ | $1/V_{32}$ |                 |
| U          | 350.0      | 541.7      | 641.4      | 444.8      | 641.4      | 641.4      | $\mu\text{s/m}$ |

## FRACTURED VISCOELASTIC MODELS

The foregoing was as purely observational (in contrast to theoretical) as the authors could make it. All of the data are shown in Figs. 7 and 8. All of the observations can be summarized by the statement that the coloured dotted lines in the two figures fit the data. Both the fit and the precision of the fit can be evaluated by inspection of the figures.

A simple physical model that is consistent with these measurements can be found in the domain of linear viscoelasticity.

The theory of linear viscoelasticity is well-established (e.g., Biot 1954; Lakes 1998; Carcione 2001; Shearer 2009). A linear viscoelastic medium satisfies a rate-dependent form of Hooke's law that can be thought of as a family of rate-dependent, complex-valued elastic tensors. A key observable for all linearly viscoelastic materials is that stiffness is an increasing function of strain rate.

While the theory was developed in full anisotropic generality, most of the literature has been directed at man-made isotropic materials. Hofmann (2006) and Sone (2012) are the only experimental studies of shales aimed at an anisotropic viscoelastic description that we know of.

A mathematically simple form of viscoelasticity that has been studied in connection with solid earth seismology (e.g., Shearer 2009 section 6.6.4) is the standard linear solid, which adds rate-dependent terms to Hooke's law and is characterized by a pair of relaxation time constants whose ratio (the relaxation ratio) is equal to the ratio between unrelaxed and relaxed moduli.

$$M^U = M^R \left( \frac{\tau_\epsilon}{\tau_\sigma} \right). \quad (13)$$

In its simplest mathematical form, a single relaxation ratio suffices for all moduli (shear, Young, bulk, etc.) though this

is not required by a physical theory. More general viscoelastic physical models can be constructed as superpositions of simple mechanisms in order to fit measured dispersion properties. In all cases, the behaviour has limiting form equation (13). Biot (1954) described a general version of the theory and treated the special case of cubic (but not transversely isotropic) media.

Comparison of equation (13) with equation (11) shows that our observed linear relationship is interpretable as a statement that  $\{C_{11}, C_{66}, C_{33}\}$  share a single relaxation ratio  $\phi$ . These three moduli, together with  $C_{13}$ , are recognized as the moduli occurring in the compressional block of the Hooke tensor.

A key observation from the reload cycles is the match between  $S_{12}$  and  $S_{13}$ . Hofmann (2006, Fig. 3.20) showed measurements of compliance as a decreasing function of frequency from 3 Hz to 800 kHz for his two shale samples. Data shown in his figure show a match between  $S_{12}$  and  $S_{13}$  similar to what we observe but he did not comment on this feature of the data.

When the condition

$$S_{12} = S_{13}, \quad (14)$$

is satisfied in a VTI medium, the compliance tensor  $\mathcal{S}$  can be written as  $\mathcal{S} = \mathcal{S}_b + \mathcal{D}$  where  $\mathcal{S}_b$  is the compliance matrix of a background isotropic medium with Young modulus  $S_{11}$  and Poisson ratio  $S_{12}/S_{33}$  and  $\mathcal{D}$  a diagonal matrix with three non-zero entries defined by

$$\mathcal{D}_{33} = B_N = S_{33} - S_{11}, \quad \mathcal{D}_{44} = \mathcal{D}_{55} = B_T = S_{55} - S_{66}, \quad (15)$$

where  $B_N$  and  $B_T$  are excess normal and tangential compliances. Under these circumstances, the number of independent moduli is reduced from five to four. It is a consequence of equations (6)–(10) that equation (14) is equivalent to:

$$(C_{13} + C_{33})(C_{13} + 2C_{66}) = C_{33}(C_{13} + C_{11}). \quad (16)$$

If any three of the four quantities  $\{C_{11}, C_{66}, C_{33}, C_{13}\}$  are specified, the fourth can be determined by enforcing equation (16).

Sayers (2008) and Sayers and Kachonov (1995) described a physical theory that associates these excess compliances with tensorial averages of excess compliances from a distribution of small, low aspect-ratio cracks. Schoenberg and Douma (1988) described an equivalent formulation that associated the excess compliances with fractures interpreted as the zero-thickness limit of thin compliant layers in an effective medium theory. We find it convenient to define the dimensionless ‘excess normal and tangential compliance ratios’

$$\chi_N = S_{33}/S_{11} \quad \chi_T = S_{55}/S_{66}. \quad (17)$$

These satisfy  $\chi_N = \mathcal{E}_N + 1 = B_N/S_{11}$  and  $\chi_T = \mathcal{E}_T + 1 = B_T/S_{66}$  where  $\mathcal{E}_N$  and  $\mathcal{E}_T$  are Schoenberg’s dimensionless excess compliances and  $B_N$  and  $B_T$  are excess normal and tangential compliances as defined by Sayers and Kachonov. We will refer to VTI media that satisfy the extra relation (14) as ‘fractured isotropic’ media. However, it is important to recognize that the excess compliance could come from a variety of physical mechanisms such as contacts between clay particles, kerogen lenses, or micro-fractures.

The above discussion applies, without need for modification, to linear viscoelastic media. If we make the reasonable speculation that condition (14), which we observed in our reload cycles, is a general property of the medium, our observed linear relationships (11) and (12) can consequently be accounted for as two additional constraints limiting the number of free parameters needed to determine the medium. Our common relaxation ratio is recognized as the relaxation ratio for the Young modulus in a background isotropic viscoelastic solid and equation (11) is equivalent to the statement that the excess compliance ratios are the same in relaxed and unrelaxed states:

$$\chi_N^U = \chi_N^R \quad \chi_T^U = \chi_T^R, \quad (18)$$

while equation (12) is equivalent to the statement that the unrelaxed excess tangential compliance ratio is equal to the relaxation ratio:

$$\chi_T^U = \phi. \quad (19)$$

Note that the first equality in equation (18) constrains the relationship between all the moduli occurring in the compressional block while the second equality in equation (18) constrains  $C_{55}$ . Our observations summarized in Table 5 only contain redundant measurements for the moduli in the compressional block and therefore should be regarded as evidence

for the first equality. The second is consistent with our data but is not tested or confirmed by any of our measurements. To the authors knowledge there is no better reference than Biot (1954) who precisely related anisotropic viscoelastic relaxation processes to experimental observables. It is beyond the scope of the present paper to delve further into the algebraic details relating our observations to relaxation operators as defined by Biot. Koppelman (1958) showed measurements on plexiglass (M33) that were fitted using a single relaxation constant.

Note also that condition equation (11) has the form of a change in physical units and implies that all dimensionless ratios between elastic constants (Poisson ratio, Thomsen parameters, velocity ratios between modes, etc) will be the same whether measured in relaxed or unrelaxed states. For example, assuming (11) and calculating the Poisson ratio:

$$\begin{aligned} \nu^U &= \frac{-S_{12}^U}{S_{11}^U} \\ &= \frac{C_{12}^U - C_{13}^U C_{13}^U / C_{33}^U}{C_{11}^U - C_{13}^U C_{13}^U / C_{33}^U} \\ &= \frac{\phi C_{12}^R - (\phi C_{13}^R)(\phi C_{13}^R / \phi C_{33}^R)}{\phi C_{11}^R - (\phi C_{13}^R)(\phi C_{13}^R / \phi C_{33}^R)} \\ &= \frac{C_{12}^R - C_{13}^R C_{13}^R / C_{33}^R}{C_{11}^R - C_{13}^R C_{13}^R / C_{33}^R} = \nu^R. \end{aligned}$$

Coining the phrase ‘special fractured viscoelastic solid’ for a linear viscoelastic medium in which both the unrelaxed and relaxed states are fractured isotropic (i.e., satisfy relations (3) and (14)) and for which the extra symmetry conditions (18) and (19) are also satisfied, we find that the density plus four independent parameters suffice to determine a complete description of the relaxed and unrelaxed elastic tensors.

One could, for example, start with axial ultrasonic velocities plus density to determine the four unrelaxed moduli  $\{C_{11}^U, C_{66}^U, C_{33}^U, C_{55}^U\}$ . Then  $C_{13}^U$  can be calculated using equation (16). Unrelaxed compliances can be calculated using equations (6)–(10). The relaxation ratio  $\phi$  can be calculated using equations (19) and (17). The relaxed moduli can be calculated using equation (11). The relaxed compliances can be calculated using equations (6)–(10).

Alternatively, one could start with an unrelaxed Young modulus and three dimensionless parameters such as the Poisson ratio, normal and tangential compliance ratios. From these one obtains the unrelaxed compliance matrix and the relaxation ratio using equations (17) and (19). The relaxed

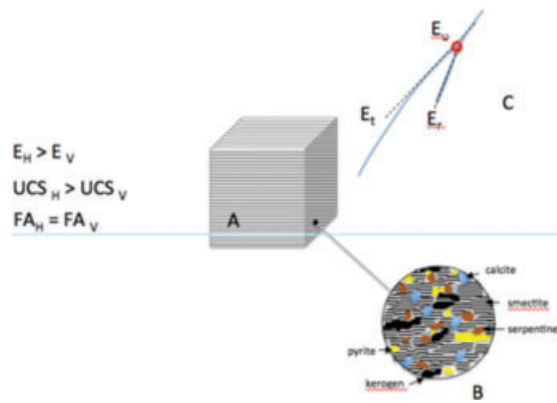


Figure 10 Conceptual geomechanical model of mudstone.

compliances and moduli can be obtained from their unrelaxed counterparts upon division by the relaxation ratio.

It is beyond the scope of the present paper to investigate these relations further. We conjecture that the Sayers/Kachanov theory, combined with a theory relating micro-friction to excess micro-compliance and the careful formalism of Biot, will be a good place to start.

## DISCUSSION

Our mudstone is a transversely isotropic rock that evidently responds in a linear viscoelastic manner to small load cycles but is inelastic when subjected to high-differential stress. A conceptual model of the mudstone and its response to stress is illustrated in Fig. 10. Figure 10(a) shows a macroscopic view of the rock including the mechanical properties of the layered VTI medium; Fig. 10(b) is a schematic of the microstructure; Fig. 10(c) is a schematic stress strain curve illustrating the mudstones response to the three loading protocols. Macroscopic layering is primarily responsible for the directional dependence on compressive strength and elastic properties. Elements governing the excess compliance comprise horizontal contacts between clay particles and horizontally aligned lenses of kerogen. At the microscopic scale, deformation is viscoelastic so long as induced shear stresses do not exceed the inter-particle frictional strength. Since smectite clay minerals are the continuous load-bearing mineral, plastic deformation should occur when the frictional strength of smectite is exceeded. When this happens the particles move past one another resulting in a low Young modulus and a non-recoverable plastic strain (Table 2).

Systematic errors in geomechanical models of mudstone are to be expected when the VTI and viscoelastic nature of the rock is not honoured. Predictions of earth stress, rock strength and wellbore stability will all be affected. Errors in wellbore

stability are compounded since earth stress and rock strength are inputs to wellbore stability models. Finally the viscoelastic nature of the mudstone affects inversion of elastic parameters from geophysical log data and the application of them in earth stress and wellbore stability models. We have seen here that the moduli for the mudstone depend on strain rate and stress level. Today these complexities are handled by calibrating geophysical logs to core measurements. A better understanding of the intrinsic rock properties that govern the mechanical properties of mudrocks will improve detection of anisotropic strata and will improve the inversion of geophysical data for rock mechanical properties and the geomechanical calculations that depend upon them (Amadei *et al.* 1897; Thiercelin and Plumb 1994).

## SUMMARY

This paper has characterized the mechanical properties of a calcareous mudstone. We presented measurements of compressive strength and static and dynamic elastic properties on a block rock retrieved from an exploration well. Measurements of mechanical properties indicate that the mudstone is anisotropic with respect to all three properties and that the magnitude of anisotropy decreases with increasing confining stress. A detailed analysis of the elastic moduli computed using small unload reload cycles and simultaneous ultrasonic wave velocities shows both strong anisotropy and strong anelasticity. Surprisingly, the measurements are consistent with a mathematical description of a special type of anisotropic linear viscoelastic medium that is obtained by adding aligned excess compliance to an isotropic viscoelastic solid. Such a material is determined by density plus four parameters defining the viscoelastic solid and the excess normal compliance associated with the cracks. The model predicts a full set of VTI parameters for both low- and high-strain rate behaviour.

The task of properly relating the statistical viscoelastic properties of a compliant microstructure to bulk observations such as ours, seems to require both a careful theory and careful experimentation. We hope our contribution moves the process forward.

## ACKNOWLEDGEMENTS

The authors are grateful to Neil Judge and Don Schultz of Hunt Oil Co. for providing the rock sample and for permission to publish the rock mechanics data. We also want to thank Herman Lemmens and Gerda Gloy of FEI Corporation for providing the mineralogical analysis. We are grateful to the assistant editor and reviewers of the original draft of

this paper, particularly to Joel Sarout who provided a very thoughtful and thorough set of comments.

## REFERENCES

- Alexandrov K.S. and Ryzhova T.V. 1961. Elastic properties of rock-forming minerals. II. Layered silicates: Bulletin of the U.S.S.R. Academy of Sciences 9, 1165–1168.
- Amadei B. 1996. Importance of anisotropy when estimating and measuring in situ stresses in rock. *International Journal of Rock Mechanics and Mining Science and Geomechanics Abstracts* 33, 293–325.
- Amadei B., Swolfs H. and Savage W. 1987. Gravity-induced Stresses in Stratified Rock Masses. *Rock Mechanics and Rock Engineering* 21, 1–20.
- Biot M.A. 1954. Theory of Stress-Strain Relations in Anisotropic Viscoelasticity and Relaxation Phenomena. *Journal of Applied Physics* 25(11), 1385–1391.
- Brown E.T. 1981. Rock Characterization Testing & Monitoring: LSRM Suggested Methods. Oxford, New York Pergamon Press. TIC Catalog Number 9663.
- Carcione J.M. 2001. Wave Fields in Real Media - Wave Propagation in Anisotropic, Anelastic and Porous Media. Elsevier 2001.
- Cheng C.H. and Johnston D.H. 1981. Dynamic and Static Moduli. *Geophysical Research Letters* 8(1), 39–42.
- Dewhurst D.N. and Siggins A.F. 2006. Impact of fabric, microcracks, and stress field on shale anisotropy. *Geophysical Journal International* 165, 135–148.
- Dewhurst D.N., Siggins A.F., Sarout J., Raven M. and Nordgard-Bolas H.M. 2011. Geomechanical and ultrasonic characterization of a Norwegian Sea shale. *Geophysics* 76(3), 101–111.
- Hofmann R. 2006. Frequency dependent elastic and anelastic properties of clastic rocks. PhD dissertation, Colorado School of Mines.
- Hornby B., Miller D., Esmersoy C. and Christie P. 1995. Ultrasonic to seismic measurements of shale anisotropy in a North Sea well. *SEG Expanded Abstracts* 14(1), 17–21.
- Hornby B.E. 1998. Experimental laboratory determination of the dynamic elastic properties of wet, drained shales. *Journal of Geophysical Research* 103, 29945–29964.
- Jackson I. 1993. Dynamic compliance from torsional creep and forced oscillation tests: An experimental demonstration of linear viscoelasticity. *Geophysical Research Letters* 20(19), 2115–2118.
- Jaeger J.C., Cook N.G.W. and Zimmerman R.W. 2007. Fundamentals of Rock Mechanics. (4th Edition). John Wiley & Sons.
- Koppelman J. 1958. Über die Bestimmung des dynamischen Elastizitätsmoduls und des dynamischen Schubmoduls im Frequenzbereich von  $10^{-5}$  bis  $10^{-1}$  Hz. *Rheologica Acta*, Nr. 1.
- Lakes R.S. 1998. Viscoelastic solids. CRC Press.
- Lo T.-W., Coyner K.B. and Toksöz M.N. 1986. Experimental determination of elastic anisotropy of Berea sandstone, Chicopee shale, and Chelmsford granite. *Geophysics* 51, 164–171.
- Lubarda V. and Chen M. 2008. On the elastic moduli and compliances of transversely isotropic and orthotropic materials. *Journal of Mechanics of Materials and Structures* 3(1), 153–171.
- Miller D., Horne S. and Walsh J. 2012. Precise Inversion of Logged Slownesses for Elastic Parameters in a Gas Shale Formation. *Geophysics* 77, B197–B206.
- Sarout J., Molez L., Gueguen Y. and Hoteit N. 2007. Shale dynamic properties and anisotropy under triaxial loading: Experimental and theoretical investigations. *Physics and Chemistry of the Earth* 32, 896–906.
- Sarout J. and Gueguen Y. 2008. Anisotropy of elastic wave velocities in deformed shales: Part I - Experimental results. *Geophysics* 73(5), 75–89.
- Sayers C.M. 2005. Seismic anisotropy of shales. *Geophysical Prospecting* 53, 667–676.
- Sayers C. 2008. The effect of low aspect ratio pores on the seismic anisotropy of shales. *SEG Expanded Abstracts* 2750–2754.
- Sayers C.M. and Kachanov M. 1995. Microcrack-induced elastic wave anisotropy of brittle rocks. *Journal of Geophysical Research* 100(B3), 4149–4156.
- Schoenberg M. and Douma J. 1988. Elastic wave propagation in media with parallel fractures and aligned cracks. *Geophysical Prospecting* 6, 571–590.
- Shearer P.M. 2009. Introduction to Seismology. (2nd Edition), Cambridge University Press.
- Sone H. 2012. Mechanical properties of shale gas reservoir rocks and its relation to the in-situ stress variation observed in shale gas reservoirs. PhD dissertation, Stanford University.
- Spencer J.W. Jr 1981. Stress relaxations at low frequencies in fluid-saturated rocks: Attenuation and modulus dispersion. *Journal of Geophysical Research* 86(B3), 1803–1812.
- Surez-Rivera R., Green S.J., McLennan J. and Bai M. 2006. Effect of layered heterogeneity on fracture initiation in tight gas shales. SPE paper, 103327.
- Thiercelin M.J. and Plumb R.A. 1994. A core base prediction of lithologic stress contrasts in East Texas Formations. *SPE Formation Evaluation* 9(4), 251–258.
- Thomsen L. 1986. Weak elastic anisotropy. *Geophysics* 51(10), 1954–1966.
- Voigt W. 1928. Lehrbuch der Kristallphysik. Johnson Reprint Corp, ISBN-10: 0384648401.